REMOTE SENSING MONITORING OF A COASTAL-VALLEY EARTHFLOW IN NORTHWESTERN GALICIA, SPAIN

Jesús Horacio[1,2]*, Efrén Muñoz-Narciso[3], Alan S. Trenhaile[4], Augusto Pérez-Alberti[1,2]

[1] Department of Geography, University of Santiago de Compostela, Galicia, Spain

[2] Laboratory of Environmental Technology (Institute of Technological Research), University of Santiago de Compostela, Galicia, Spain

[3] Department of Environment and Soil Sciences (DMACS), Universitat de Lleida, Catalunya, Spain

[4] Department of Earth and Environmental Sciences, University of Windsor, ON, Canada

* Corresponding author. Email: horacio.garcia@usc.es Phone: (+0034) 981·563·100 (ext. 12591)

Abstract

Historical air photographs, LiDAR, and an unmanned aerial vehicle (UAV) were used to record the movement, from 1956 to 2018, of a clay and clast earthflow in a coastal valley in northwestern Spain. Two procedures were employed. The first tracked changes, in a GIS environment, in the location of eight, easily identified objects on the surface of the deposit (large boulders, topographic lobes, and the foundations of an old hut). The second used DEMs of Difference (DoDs) based on Digital Elevation Models from a 2010 LiDAR flight and two UAV flights in 2016 and 2018 obtained by Structure from Motion-Photogrammetry techniques. While the first procedure provided estimates for earthflow movement over a 62-year period, the second produced more precise data for periods of up to 8-years. The first procedure indicated that the mean rate of movement was 0.48 m·yr^{-1}, increasing from only 0.14 m·yr^{-1} from 1956 to 1983 to between 0.50 and 0.83 m·yr^{-1} from 1983 to 2018. Despite some temporal and spatial changes in direction, rates of surface movement were quite uniform on the deposit. The increase in earthflow movement after 1983 may be related to an increase in rainfall, although human activities associated with the removal of a wrecked ship from the nearshore may have been a contributing factor. The role of debuttressing due to the wave-induced removal of lateral support from the toe of the deposit is less clear. While there was no clear relationship between wave erosion and rates of movement, coastal retreat may have triggered changes in the

direction and sediment flux in the toe of the deposit. This effect could have been tempered by negative feedback, however, whereby coastal erosion and increased flow activity were countered by the protection afforded by the accumulation of large, dislodged boulders on the beach. Because of this feedback, it is difficult to predict the impact of sea level rise and other elements of climate change along this coast.

Keywords: earthflow, coastal-valley, UAV, LiDAR, SfM-Photogrammetry, Galicia.

1. Introduction

Steep slopes produced by marine undercutting are conducive to many types of mass movement in coastal regions. The type, size, and frequency of these movements, and subsequently the rate and mode of cliff evolution and sediment supply to the coast, reflect the absolute and relative efficacy of the subaerial and marine process suites. The importance of these mechanisms varies according to the climate, which drives marine and subaerial processes, and the structure and other characteristics of the rock, which determine their resistance to weathering and erosion (Vann Jones et al., 2015; Hampton and Griggs, 2004; Sunamura, 1992; Trenhaile, 1987; Emery and Kuhn, 1982).

Rockfalls triggered by marine undercutting are dominant on many exposed coasts, but translational and rotational landslides can predominate where geological conditions are suitable. Earthflows are intermittent slope movements of plastic, clayey soils that can develop at the bulbous front of slumps or at the foot of steep, eroding cliffs. They are generally less common than falls and slides on rocky coasts, although they can develop from landslides or other loose debris where water flows are concentrated on the floor of short, steep valleys.

Flows in coastal areas vary according to their morphology, topography, rheology, and sedimentology (Germain and Ouellet, 2013). Material moves within earthflows as a result of the intermittent flow-like movement of plastic, clayey soil, internal shear strains, and sliding along single or multiple shear surfaces. This produces lobate structures with typical rates of movement ranging, from meters per hour during active periods to meters per year in general (Hungr et al., 2014; Keefer and Johnson, 1983; Varnes, 1978).

Whereas many mass movements are rapid and can only be examined after they have occurred, they can be measured and monitored in slow earth flows as they take place. There have been notable advances in recent years in our ability to retroactively identify and measure slow changes in topographic elements. They include developments in geomatics (e.g. TPS, GPS-RTK, TLS), remote sensing (high resolution satellite images, Airborne-LiDAR), and photogrammetry (automated digital photogrammetry, unmanned aerial vehicle –UAV–). The newest techniques, often involving Structure from Motion-Multi View StereoScan (SfM-MVS onwards) and UAVs, produce low cost and high quality-quantity topographical information. This

technology plays a key role in assessing, monitoring, and analysing global change and, accordingly, there has been an exponential increase in their use in the geomorphological disciplines, including mass movements (Turner et al., 2015; Abellán et al., 2014; Lucieer et al., 2014; Daehne and Corsini, 2013; Niethammer et al., 2012; Prokop and Panholzer, 2009; Baldi et al., 2008) and coasts (Castelle et al., 2017; Sturdivant et al., 2017; Autret et al., 2016; Casella et al., 2016; Ierodiaconou et al., 2016; Turner et al., 2016; Gonçalves and Henriques, 2015; Pérez-Alberti et al., 2015a,b; Harwin and Lucieer, 2012; Delacourt et al., 2009).

The purpose of this paper is to discuss the earthflow-like movement of debris on the northwestern coast of Spain. More specifically, it is concerned with spatial and temporal changes to slope behavior, including to rates of movement at annual to decadal scales, and the interaction between terrestrial mass movement and marine erosional processes. Historical air photographs, LiDAR, and images obtained with an UAV and SfM-MVS techniques were used to identify temporal and spatial changes in rates of movement in the distal fan or lobate debris cone over a 61-year period. This was supplemented by precipitation and wave data to relate these changes to a variety of environmental conditions. The research was conducted in a rocky coastal-valley environment, and therefore differs from previous attempts to record temporal and spatial patterns of movement in slow mass movements (Handwerger et al., 2015; Prokešová et al., 2014; Mackay and Roering, 2011; Coe et al., 2009) in that wave erosion and the removal of lateral support from the toe of the flow must be considered in addition to variations in rainfall intensity and frequency. Additionally, although this earthflow is a locally significant source of sediment on a slowly eroding coast, its size is constrained by the high coastal cliffs in the study area and by the correspondingly short length and small catchment area of the valley that is incised into them. This earthflow is therefore much smaller than the long earthflows frequently described in more terrestrial environments (Keefer and Johnson, 1983; Handwerger et al., 2015). The terms *deposit*, *debris lobe* and *flow* are used in places to refer to the earthflow in this paper, with the latter term used to refer to its movement, irrespective of whether it is accomplished primarily by sliding or flowing.

2. Study site

The study was made in northwestern Galicia, Spain, in a region considered to be of such geological, pedological, archeological, and biological interest that it has been proposed as a future Geopark, a legal designation under the auspices of UNESCO. The climate of this region is humid oceanic, with abundant precipitation (~2,000 mm per year) and mild temperatures (~14 °C), punctuated with microclimates related to slope aspect and proximity to the ocean.

The study was concerned with the lower portion of an unnamed valley (henceforth referred to as the Teixidelo valley) terminating at the rear of an adjacent boulder beach, about 1.8 km east of the village of Santo André de Teixido (Fig. 1A). The valley has been incised into a cliff cut into a gently sloping plateau (with cliff-top gradients < 8º to 16º). The cliffs in this region have a maximum elevation of 612 m (Vixía Herbeira), and are among the highest on the European mainland. The cliff face is generally steep, with gradients ranging up to the sub-vertical in places. The valley is oriented perpendicularly to the shore and is about 1 km in length. It is steep and narrow in the header zone but more gently sloping (20 to 30º) and wider nearer the coast. The valley runs along a NW-SE oriented fault with a 65ºdip, which was formed during an extensional phase in the Variscan orogeny. The rocky substratum in the valley consists of ultramafic, granulitic and phyllonian quartz rocks (Fig. 1B).

The floor of the valley is occupied by a bulbous, hummocky deposit, about 200 m in length (Fig. 1A and Fig. 2A). Active and inactive sections of the deposit were identified according to the occurrence of slope fissures and related scarps (Fig. 1), and by distinguishing between elements (e.g. large boulders) that are moving from those that are not, based on remote sensing data. Air photographs show that several boulders further up the valley have been stationary since at least 1956, and that this essentially inactive section does not contribute to movement in the debris lobe further seawards. Two subareas can be distinguished in the active zone. The upper one, extending seawards from the head of the active zone, has many cracks, gullies, and other breaks in the soil cover of various shapes and dimensions, and a scarp composed of clay which forms the base of the moving mass (Fig. 2B). The second area, further seawards, is an accumulation zone containing numerous boulders of different sizes, and diverse lobes, indicative of multiple shear surfaces, moving toward the sea, where it is exposed to, and periodically truncated by, storm waves (Fig. 2C and 2D).

Data from field measurements and LiDAR based DEMs (Digital Elevation Models) suggest that the deposit is variable in thickness, being about 13 m in the central part of the flow and as much as 20 m in the southern sector. There are linear ridges running along its sides, parallel to the valley, and curved, transverse ridges in the lower, central part. Most of its surface is covered by grass and small bushes, with some willows (*Salix sp.*) and hazels (*Corylus avellana*) at the head of the valley. The deposit contains angular and subangular rock fragments ranging up to large boulders with their major axes > 3 m (Fig. 2E). These clasts are in a greenish-gray montmorillonite clay matrix that is rich in magnesium phyllosilicates and very plastic when saturated. The rock fragments in the deposit are representative of the local valley substrata, including granular amphibolites and intensely fractured pyroxenite-peridotites, with a predominance of amphibolites on the southern side of the valley and pyroxenite-peridotites on the northern side.

3. Methods

The basic data used to monitor movements in the valley-floor deposit were obtained from aerial surveys (Table 1). Orthophotographs were available for 1956, 2008, 2010, 2014, and 2017 and for LiDAR in 2010. Other air photographs from 1945, 1983, 1984, 2002, and 1990, were rectified for this study. All images from the period 1945-2014 and 2017 were obtained from the relevant state organism (The National Geographic Institute and, for 1945, the Cartographic and Photographic Center). Additional high resolution data were obtained in 2016 and 2018 using a low flying UAV (Tables 1 and 2). Because of their resolution and low quality, it was concluded that the 1945, 1984, and 2002 images should not be used in this paper, and that 1956 would therefore represent year zero for this study.

Two procedures were used to quantify movement in the valley deposits. The first was concerned with locating and recording the position in a GIS environment of the centroid of selected features on the valley floor, on a two-dimensional xy plane. A variable scale (a maximum from 1/60 in 2016 and a minimum of 1/500 in 1956) was used to map the location of these features on each image in order to identify and compare changes in their location through time. The same line and polygon were used for all the images; both shapes (line and polygon)

were drawn using the highest quality image (2016). The features that were selected were clearly recognizable and re-locatable on the studied images, including large boulders (clasts, referenced as C1 to C4) and topographic lobes (referenced as L1 to L3) with well-defined ridges (Fig. 4). The only anthropogenic feature was the stone wall base of a small, ruined building (henceforth referred to as a hut), which was constructed for a former nickel mining operation. Peak activity was in the mid-nineteenth century and mining ceased at the end of the 19th century. The location of the coast was represented on the images by a well-defined, erosional scarp which forms the front of the debris lobe (Fig. 2E). Mean rates of movement over specified time periods are given to two decimal points. This does not represent the degree of measurement precision, which varies with the particular aerial survey, but is rather the product of dividing the amount of movement over a period by the corresponding time interval.

The second procedure was based on the DEM of Difference (DoD) produced from DEMs from the 2010 LiDAR flight and the 2016 and 2018 UAV flights. Georeferencing of the UAV data was based on 38 (2016 flight) and 19 (2018 flight) ground control points measured using GIobal Positioning System - Real Time Kinematics (GPS-RTK) and a Total Station (total RMSE - the root mean square error - 3 cm) (Table 2). Density and spatial distribution of the ground control points followed previous studies to try to obtain the lowest RMSE (Vericat et al., 2009). The data were processed using Agisoft PhotoScan Pro 1.2.6 software. An orthoimage with 10 cm spatial resolution was generated as a by-product of the SfM-MVS technique (Gonçalves and Henriques 2015; Turner et al. 2015). This second procedure provided a more precise estimate of the rate of movement than the first procedure, although it was representative of only a much shorter time frame (8 yrs). ArcGIS 10.5 software and a version of the Toolbox Geomorphic Change Detection (GCD) developed by Wheaton et al. (2010), was used on the DoDs to identify and map changes in the total and relative elevation, area, and volume of the earthflow, and consequently to calculate the net sedimentary balance in the study area. LoDMin of ± 25 cm was used for the Minimum Level of Detection (LoDMin), the smallest change in elevation that can be detected in the topographic models, based on the RMSE of the check points of the DEMs.

There were no continuous precipitation records from the study area, so one was compiled by combining data from four stations in adjacent areas (Table 3). Daily rainfall and the cumulative

deviation from the mean of daily rainfall were used to provide a measure of variation over the study period (Massey et al., 2013). Deep-seated earthflows often require prolonged periods of precipitation, however, in order to raise pore-water pressures sufficiently to trigger movement along the basal shear zone (Handwerger et al., 2015). Therefore, to consider the effect of persistent and heavy rainfall events, five-day and ten-day running totals were calculated for the entire study period.

Wave data were obtained from the National Oceanographic Institute (Puertos del Estado). Although there is a buoy at Estaca de Bares, about 44 km from the study area, it has only been operating since 1996 and there are significant gaps in the record. Consequently, simulated data were used in this study from SIMAR point 3036042, only about 4 km from the study area. These data represent a temporal (hourly) series of wind, surf, and sea level parameters derived from numerical models rather than from direct measurement of wave conditions (Gómez-Lahoz and Carretero-Albiach, 2005). Because the SIMAR data only extend back to 1958, data were lacking for the period of study from 1956-10-13 to 1957-12-31. The SIMAR data used in this study were spectral significant wave height and mean direction. The National Oceanographic Institute considers that SIMAR data provide adequate descriptions of actual wave conditions for almost all parts of Spain. This was confirmed for northern Galicia through an analysis conducted in the present study, which found that there was a high correlation (non-parametric Spearman's rank correlation coefficient 0.92) between modeled (SIMAR 3036042) and recorded mean daily significant wave height at the Estaca de Bares buoy. Nevertheless, there was a tendency, possibly related to differences in the physical characteristics of the buoy and the simulation site, for the model to underestimate the height of the highest waves (Fig. 3). Variations in wave conditions were represented in the present study by changes in the maximum daily wave height over the study period, and in the daily frequency of waves of more than 8 m in height.

Coastal erosion periodically trims back the base of the earthflow, removing lateral support (debuttressing) and possibly promoting more rapid movement of the wet, plastic debris (Fig. 2E and 2F). To assess the effect of this factor, changes in the location of the erosional bluff or, following a period of deposition, the leading edge of the flow, were recorded over each of the survey periods at ten locations (lines) spaced approximately 24 m apart along the coast. These

211 data were then compared with the rates and direction of movement of the deposit recorded over
212 the same periods.

213

214 ## 4. Results

215 Based on the DEM of the 2010 LiDAR survey and the tool Surface Volume (ArcMap 10.5), the
216 volume of the mobile deposit on the floor of the Teixidelo valley is about 11 x 10^6 m^3, compared
217 with the 48 x 10^6 m^3 volume of the valley and the 172 x 10^6 m^3 of the much larger scar which
218 encloses the valley and a large deposit on its eastern side (Fig. 1A). These estimates suggest
219 that, assuming the deep valley was the source of the material in the earthflow, about 94 % of
220 the material eroded and transported from the valley, by mass movements or by fluvial or even
221 glacial mechanisms (Pérez-Alberti, 2014), has been removed already by the sea. Conversely, if
222 the mobile deposit was derived entirely from the Teixidelo valley, then about 77 % of the
223 material would have been removed.

224 The mean rate of movement since 1956 for the eight recorded points, was 0.48 m yr^{-1}, which
225 has resulted in a displacement of about 30 m down the valley (Table 4, Fig. 4A). Mean rates
226 increased from only 0.14 m·yr^{-1} from 1956 to 1983, to between 0.50 and 0.87 m·yr^{-1} from 1983
227 to 2018. The mean rates, and consequently the corresponding distances of travel, have been
228 broadly similar for each of the eight monitored points over the study period, ranging between
229 only 0.43 and 0.50 m·yr^{-1} (Table 4). There was no consistent trend in the rates of movement in
230 this area from the rear to the front of the deposit. For example, although the most landward
231 points, C1 and L1, had slightly higher overall rates of movement than the most seawards, L2
232 and L3, from 1956 to 2018, the landward and seaward rates varied, relative to each other, from
233 1956 to 1983 and 1983 to 2018.

234 Although there were some temporal and spatial changes, the general direction of movement
235 was north-northwesterly over the monitoring period. The most significant changes, involving a
236 slight shift of the centroids to the west before the flow reverted to its former direction, were by
237 C1, C2, and C3 between 1983 and 1990, and a change to a more westerly direction by several
238 tracked points, but especially by L2 and L3, between 2016 and 2018 (Table 5, Fig. 4B).

239 Based on the DoDs from the 2010 LiDAR and the 2016 and 2018 UAV surveys, most of the
240 debris lobe experienced positive or negative changes in elevation, ranging up to almost 5 m
241 from 2010 to 2016 and almost 4 m from 2016 to 2018 (Fig. 5 and Fig. 6). The changes were
242 broadly similar over the two periods, with surface elevation dominating in the depletion zone in
243 the southern interior. Areas of surface lowering and elevation coexisted in the outer,
244 accumulation zone, across the toe of the deposit (Table 6, Fig. 5 and Fig. 6). These areas were
245 distributed in an irregular but broadly crescentic pattern parallel to the front, forming an
246 undulating surface, although the prominent band which experienced a loss in elevation was
247 more continuous and wider in 2010-2016 than in 2016-2018 (inset C provides a detailed view of
248 a section of this band in Figs. 5 and 6). The crescentic pattern was punctuated by a few ridges
249 running parallel to the direction of movement, along either side of the deposit. These ridges
250 were increasingly elevated between 2010 and 2016 and in general from 2016 to 2018, although
251 a few experienced some lowering during this latter period. Another distinctive area, around a
252 very large boulder (C4) near the western edge of the deposit, experienced slight uplift from
253 2010 to 2016 but was characterized by an irregular, essential random patchwork of elevated
254 and depressed areas from 2016 to 2018 (inset map A in Fig. 5 and Fig. 6).

255 The heaviest rainfall, based on the number of days each year in which there was more than 70
256 mm, occurred during several periods between 1991 to 2018, and particularly from 1983 to 1991
257 when the area experienced the remnants of Hurricanes Klaus and Hortensia in 1984, and an
258 intense NW storm in February 1989 (Fig. 7A). Cumulative deviation from the daily mean rainfall
259 was generally below the mean from 1957 to 1985 and above it, attaining a maximum around
260 2004, from 1986 to 2018 (Fig. 7A). The most frequent high rainfall events, totaled over 5-day
261 and 10-day periods were between 1983 and 1990 and from 2014 to 2016 (Table 7).

262 Maximum daily, monthly, and annual wave heights were broadly similar over the entire study
263 period (1958-2018), although the extreme values (frequency of waves > 8 m) were a little higher
264 in the period before than after 1990, and especially between about 1984 and 1990 (Fig. 8). The
265 coast experienced periods of erosion and deposition during the monitoring period, varying in
266 space and time, with faster rates of wave erosion generally occurring over shorter periods than
267 slower rates of earthflow-induced deposition. Consequently, there were only fairly minor long-
268 term changes in the position of most of the shore along the front of the debris lobe, with the

exception of marked erosion in the east-central portion (lines 7 to 9), where the coast has retreated from almost 16 m to more than 22 m since 1956 (Fig. 9).

There was little evidence, based on a comparison of erosion rates during periods of coastal erosion and deposition, to suggest that debuttressing has caused rates of movement to increase. The hut and lobes L2 and L3 are only about 20-25 m from the coast and might therefore be expected to respond to debuttressing. The hut is almost directly behind coastal line 7, which has experienced almost continuous coastal erosion and retreat since the 1983-1990 period. Conversely, L2 is behind line 6 and L3 is between lines 4 and 5, which have experienced offsetting periods of coastal advance and retreat over the study period (Fig. 4B and Fig. 9). The mean rate of movement of the hut was a little higher than for L3, despite the occurrence of more than 3 m of erosion on line 5 between 2005 and 2008 when, paradoxically, the rate of movement at L3 declined, and mean rates were identical for the hut and L2 (Table 4). Similarly, coastal erosion did not appear to be responsible for higher rates of movement than deposition over each monitoring interval. For example, L2 and L3 experienced high rates of movement (1.04-1.37 $m \cdot yr^{-1}$, respectively) during a period of coastal stability or only minor erosion in their adjacent coastal zones from 2017-2018, and low rates of movement (0.49-0.32 $m \cdot yr^{-1}$, respectively) during a period of erosion in these coastal zones from 2005-2008. The general lack of a direct relationship between rates of earthflow movement and coastal erosion is also consistent with the lack of a response by hut movement to about 2.5 m of coastal erosion along line 8 from 2017-2018 (Fig. 9).

Despite the lack of a clear relationship between rates of movement and coastal erosion, other evidence suggests that debuttressing may have an effect on earthflow dynamics. Rates of earthflow movement generally decrease towards the toe (Keefer and Johnson, 1983). The tendency for rates to be fairly uniform from the rear to the front of the Teixidelo earthflow (Table 4) is therefore atypical, and may imply that truncation and undermining of the deposit by coastal erosion help to draw it downslope, thereby facilitating movement in the seaward extremity at rates that are higher than would otherwise occur. Debruttressing may also have influenced the direction of earthflow movement, as plastic debris was diverted away from coastal areas that were stable or advancing seawards towards adjacent areas that were eroding. There is some evidence to support this contention in the study area. For example, the more than 3 m of

299 erosion that occurred between 2005 and 2008 along coastal line 5 may explain why L3 swung
300 towards (41º) the northeast. Conversely, while L2 swung away from line 5, it moved north-
301 northeasterly (19º) towards line 7, which had been experiencing almost continuous, albeit minor,
302 erosion since 1983 to 1990 (Table 5, Fig. 4B and Fig. 9). Nevertheless, other changes cannot
303 be attributed to coastal erosion. They include those by C1, C2, and C3 in the southern and
304 eastern interior of the flow between 1983 and 2005, which were probably generated by internal
305 pressures, and other directional changes over short distances that likely resulted from rotation
306 of the tracked points on the flow and resulting changes in the location of the associated
307 centroids.

308

309 ## 5. Discussion

310 This study has been concerned with decadal-scale monitoring of patterns and rates of
311 movement in a coastal earthflow, using historical air photographs and high resolution LiDAR
312 and UAV-based airborne systems. While remote sensing is a valuable tool to monitor long-term
313 changes in coastal systems, including earthflows and other slow mass movements, the
314 temporal resolution is too coarse to provide definitive evidence of the responsible mechanisms,
315 which operate over much shorter timescales. Valuable inferences can be drawn, however, from
316 the morphology of the deposit, temporal and spatial variations in flow dynamics, and
317 meteorological and oceanographic data on rainfall and wave heights. Remotely sensed data in
318 coastal regions can therefore be used to identify and focus on areas of particular interest for
319 more detailed field study, to estimate rates of coastal retreat and the contribution of mass
320 movements to coastal sediment budgets, and to assess the possible risks posed to coastal
321 communities and infrastructure by rising sea level and increased storminess.

322 The mobile deposit in the Teixidelo valley can be described, according to the classification of
323 Hungr et al. (2014), as a slow earthflow. This conclusion is consistent with its morphology, the
324 different directions and overall rates of movement, and the presence of a clay matrix which is
325 very plastic when saturated. The flow-parallel ridges running along the sides of the deposit are
326 fairly common features on earthflows (Keefer and Johnson, 1983). As they are generally still
327 rising in this area, (Fig. 5 and Fig. 6) and are covered in vegetation, they are probably the

328 product of internal pressures generated within the flow, rather than of material overflowing onto
329 the adjacent ground surface. It is generally accepted that earthflows, as well as other types of
330 mass movement, are triggered and are therefore most prevalent during periods of high rainfall.
331 The relationship in the study area between rates of movement and increases in the occurrence
332 of heavier rainfall in the 1980s is therefore predictable and consistent with the literature (Table
333 7, Fig. 7B) (Bayer et al., 2018; Hürlimann et al., 2016; Handwerger et al., 2015; Giordan et al.,
334 2013; Massey et al., 2013; Keefer and Johnson 1983). Nevertheless, because only 9 time
335 intervals were available for this study, Spearman's rank correlations (ρ) were insignificant for
336 rates of earthflow movement against: time (ρ 0.23; P 0.55); rainfall (number of cumulative 5-day
337 rainfall events > 70 mm) (ρ 0.13; P 0.75); and storm frequency (number of large storms with
338 waves > 8 m) (ρ 0.11; P 0.78). An anthropogenic event may also have triggered an increase in
339 debris mobility in this area, although it cannot account for the continuation of similar rates of
340 movement more than 3 decades later. This occurred in January 1986, when the 185 m-long
341 freighter Bonnie Carrier ran aground directly in front of the Teixidelo valley. The wreck created a
342 barrier against wave attack and its subsequent removal required construction of an extensive
343 track system in the valley which destabilized the deposit in places (Fig. 10).

344 In a coastal environment, one might also expect rates of earthflow movement to increase
345 following periods of wave-induced erosion and destabilization of the slope deposits. There is no
346 direct evidence that wave erosion is responsible for increased rates of movement of the
347 Teixidelo earthflow, although this effect may have been obfuscated by the fairly low temporal
348 resolution of the remotely sensed data. Given that rates of movement generally decrease down
349 earthflows (Keefer and Johnson, 1983), the occurrence of quasi-uniform rates may be indicative
350 of the lack of a lower, slower moving section due to the proximity of the coast, or it could be the
351 result of debuttressing by wave erosion. Erosional truncation of the earthflow and the presence
352 of a steep scarp at the coast suggest that both of these factors must be significant (Fig. 2D and
353 2E). While wave erosion probably promotes increased output from the terrestrial to the littoral
354 system, however, the effect may be short-lived due to the greater protection from the waves
355 afforded by the large, essentially immobile boulders dislodged from the flow, which accumulate
356 at the cliff foot (Fig. 2F). According to this hypothesis, coastal earthflows containing significant
357 amounts of coarse material may experience cyclical perturbations in activity that are

358 superimposed on those due to precipitation. The amplitude and frequency of these cycles will
359 reflect the amount of protective material at the cliff foot and its rate of removal, which will
360 depend, in turn, on such factors as the wave climate, the thickness of the earthflow toe, and the
361 amount and size of the coarse material in it (Fig. 11).

362 The toe of the earthflow extends along the coast for about 215 m, and its mean height at the
363 shore is 11.2 m (Fig. 2D and 2E). Based on measured rates of earthflow movement (Table 4)
364 and estimates that coarse material constitutes roughly 20 % of the sediment (Fig. 2E), the flow
365 will have contributed more than 14,000 m^3 of coarse sediment to the littoral budget since 1956
366 and almost 13,000 m^3 since 1983; this corresponds to an annual supply of 1.1 m^3 and 1.7 m^3 of
367 debris per 1 m of coast, respectively. Fine material in the earthflow erodes fairly continuously
368 but it is carried offshore in suspension, whereas the erosion of coarse material, which stays on
369 the beach, is more episodic. Because these erosional events tend to be of high magnitude and
370 low frequency, clast accumulation and removal is likely to produce temporally and spatially
371 variable amounts of toe protection, and consequently rates and directions of earthflow
372 movement.

373 Rock coasts are generally expected to experience more rapid rates of erosion with climate
374 change. There are many possible complexities however which could trigger differences in
375 coastal response in space and time. Rising sea level and possibly increased storminess will
376 trigger attendant changes in wave refraction patterns, tidal range and sediment production,
377 transport and accumulation, while changes in temperature and precipitation will affect coastal
378 mass movements, weathering rates and bioprotectional and bioerosional processes; these
379 complex, interacting mechanisms could act to increase erosion rates in some areas and
380 decrease them in others (Trenhaile, 2014). The results of the work described in this paper
381 suggest that the composition of coastal earthflows will have important implications regarding
382 their response to climate change and their ability to provide sediment to the littoral environment.
383 Climate change may lead to increased precipitation in some places, and consequently greater
384 earthflow activity, while higher sea level and increased storminess will promote wave erosion
385 and changes in the water table and pore water pressures. These effects may be countered in
386 some types of earthflow by the accumulation of coarse sediment on the beach, but the

protective effect is likely to be insignificant where the material is dominantly fine-grained and able to be transported offshore in suspension.

6. Conclusions

The main conclusions of this paper are:

a. Mean rates of movement of the coastal earthflow in the Teixidelo valley increased from 0.14 $m \cdot yr^{-1}$ between 1956 and 1983 to between 0.50 and 0.83 $m \cdot yr^{-1}$ from 1983 to 2018.

b. The increase in transport rates corresponded to, and was presumably largely a result of, an increase in precipitation.

c. Despite the general lack of a relationship between transport rates and coastal erosion, other evidence suggests that debuttressing may promote downslope sediment flux and trigger changes in direction.

d. The movement of coastal earthflows containing large quantities of coarse material may be constrained by negative feedback, whereby erosionally induced debuttressing and faster earthflow movement results in greater accumulation of coarse, protective debris on the beach and, subsequently, reduced rates of coastal erosion.

Acknowledgements

The authors thank Ramón Blanco Chao 'Mochi', Dominic Royé, Alejandro Gómez Pazo, Víctor Bouzas Blanco, Sam McColl, Miguel San Claudio Santa Cruz and Pilar Gil (National Oceanographic Institute) for their suggestions and efficient solutions to our technical questions. To the entire team at the National Geographic Institute for public relations for their kindness and efficiency in the request of information and clarification of doubts. To Francisco Canosa 'Fran', geologist and main promoter of the proposal for a Geopoark at the study site, for the relevant geological and historical information offered. He also provided the photo in Figure 2B. To José Manuel Freire Roca (Xestega Delineación S.L. Company) for providing,

topographic material without charge. To Bárbara Barrientos Low, María del Rosario Ibarra Ibarra and Marta Franch Sas for their diverse help. We especially thank José Manuel Sierra-Pernas 'Chema' for his support in the field and for office and logistics work, as well as his valuable comments to improve the article.

We also thank the anonymous reviewers for their comments and suggestions.

The first author is a beneficiary of the post-doctoral fellowship named *Programa de ayudas de apoyo a la etapa inicial de formación posdoctoral (2017)* founded by the *Consellería de Cultura, Educación e Ordenación Universitaria de la Xunta de Galicia* (Government of Galicia, Spain).

The second author is a beneficiary of the pre-doctoral fellowship FPU 13/00168 founded by the Ministry of Education, Culture and Sport of Spain.

References

Abellán, A., Oppikofer, T.,Jaboyedoff, M., Rosser, J.N., Lim, M., Lato, J., 2014. Terrestrial laser scanning of rock slope instabilities. Earth Surf. Process. Landf. 39 (1), 80–97.

Autret, R., Dodet, G., Fichaut, B., Suanez, S., David, L., Leckler, F., Filipot, J. F. (2016). A comprehensive hydro-geomorphic study of cliff-top storm deposits on Banneg Island during winter 2013–2014. Marine Geology, 382, 37–55. https://doi.org/10.1016/j.margeo.2016.09.014.

Baldi, P., Cenni, N., Fabris, M., Zanutta, A., 2008. Kinematics of a landslide derived from archival photogrammetry and GPS data. Geomorphology 102, 435–444.

Bayer, B., Simoni, A., Mulas, M., Corsini, A., Schmidt, D., 2018. Deformation responses of slow moving landslides to seasonal rainfall in the Northern Apennines, measured by InSAR. Geomorphology 308, 293–306.

Casella, E., Rovere, A., Pedroncini, A., Stark, C. P., Casella, M., Ferrari, M., & Firpo, M. (2016). Drones as tools for monitoring beach topography changes in the Ligurian Sea (NW Mediterranean). Geo-Marine Letters, 36(2), 151–163. https://doi.org/10.1007/s00367-016-0435-9.

Castelle, B., Bujan, S., Ferreira, S., Dodet, G., 2017. Foredune morphological changes and beach recovery from the extreme 2013/2014 winter at a high-energy sandy coast. Mar. Geol. 385, 41– 55.

Coe, J.A., McKenna, J.P., Godt, J.W., Baum, R.L., 2009. Basal-topographic control of stationary ponds on a continuously moving landslide. Earth Surf. Process. Landf. 34, 264–279.

Concello de Cariño (2010). Patrimonio e desenvolvemento local: reflexións e iniciativas no Concello de Cariño. Actas das I e II Xornadas de Patrimonio e Desenvolvemento Local. Concello de Cariño, 154 p.

Daehne, A., Corsini, A. 2013. Kinematics of active earthflows revealed by digital image correlation and DEM subtraction techniques applied to multi- temporal LiDAR data. Earth Surf. Process. Landforms 38, 640–654.

Delacourt, C., Allemand, P., Jaud, M., Grandjean, P., Deschamps, A., Ammann, J., Cuq, V., Suanez, S., 2009. DRELIO: an unmanned helicopter for imaging coastal areas. J. Coastal Res. Spec. Issue 56, 1489–1493.

Emery, KO., Kuhn, GG. 1982. Sea cliffs: their processes, profiles, and classification. Geol. Soc. Amer. Bull. 93, 644–54

Germain, D., Ouellet, M.-A. 2013. Subaerial sediment-water flows on hillslopes: Essential research questions and classification challenges. Progress in Physical Geography: Earth and Environment 37, 813–833.

Giordan, D., Allasia, P., Manconi, A., Baldo, M., Santangelo, M., Cardinali, M., Corazza, A., Albanese, V., Lollino, G., Guzzetti, F. 2013. Morphological and kinematic evolution of a large earthflow: The Montaguto landslide, southern Italy. Geomorphology 187 (2013) 61–79.

Gómez-Lahoz, M., Carretero-Albiach, J.C. (2005). Wave forecasting at the Spanish coasts. Journal of Atmospheric and Ocean Science, 10(4): 389- 405. DOI: 10.1080/17417530601127522.

Gonçalves, J.A., Henriques, R., 2015. UAV photogrammetry for topographic monitoring of coastal areas. ISPRS J. Photogramm. Remote Sens. 104, 101–111.

Hampton, M.A., Griggs, GB. 2004. Formation, Evolution, and Stability of Coastal Cliffs – Status and trends. United States Geological Survey. Professional paper 1693.

Handwerger, AL., Roering, JJ., Schmidt, DA., Rempel, AW. 2015. Kinematics of earthflows in the Northern California Coast Ranges using satellite interferometry. Geomorphology 246, 321–333.

Harwin, S., Lucieer, A., 2012. Assessing the Accuracy of Georeferenced Point Clouds Produced via Multi-View Stereopsis from Unmanned Aerial Vehicle (UAV) Imagery. Remote Sensing 4, 573-1599. ; DOI: 10.3390/rs4061573.

Hungr, O., S. Leroueil, and L. Picarelli. 2014. The Varnes classification of landslide types, an update. Landslides 11:167–194.

Hurlimann, M., Lantada, N., Gonzalez, M., Pinyol, J. 2016. Susceptibility assessment of rainfall-triggered flows and slides in the Central-Eastern Pyrenees. A: International Symposium on Landslides. Landslides and Engineered Slopes. Experience, Theory and Practice: Proceedings of the 12th International Symposium on Landslides (Napoli, Italy, 12-19 June 2016). Napoli: CRC Press, Aversa, S. (ed.), p. 1129-1136.

Ierodiaconou, D., Schimel, A. C. G., & Kennedy, D. M. (2016). A new perspective of storm bite on sandy beaches using Unmanned Aerial Vehicles. Zeitschrift Für Geomorphologie, Supplementary Issues, 60(3), 123–137. https://doi.org/10.1127/zfg_suppl/2016/00247

Keefer, DK., Johnson, AM. 1983. Earth Flows: Morphology, Mobilization, and Movement. US. Geological Survey Professional Paper 1264 United States Government Printing Office, Washington.

Llena, M., Vericat, D., Martínez-Casasnovas, J.A. (2018) Aplicación de algoritmos Structure from Motion (SfM) para el análisis histórico de cambios en la geomorfología fluvial. Cuaternario y Geomorfología, 32 (1- 2): 53-73.

Lucieer, A., De Jong, S.M., Turner, D., 2014. Mapping landslide displacements using structure from Motion (SfM) and image correlation of multi-temporal UAV photography. Prog. Phys. Geogr. 38 (1):97–116. http://dx.doi.org/10.1177/0309133313515293.

Mackay, B.H., Roering, J.J., 2011. Sediment yield, spatial characteristics, and the long-term evolution of active earthflows determined from airborne LiDAR and historical aerial photographs, Eel River, California. Geol. Soc. Amer. Bull. 123, 1560-1576.

Massey, CI., Petley, DN., McSaveney, MJ., 2013. Patterns of movement in reactivated landslides. Engineering Geology 159, 1–19.

Niethammer, U., James, M.R., Rothmund, S., Travelletti, J., Joswig,M., 2012. UAV-based remote sensing of the Super-Sauze landslide: evaluation and results. Eng. Geol. 128, 2–11.

494 Pérez-Alberti, A., 2014. Geomorfología, in: Ferreiro, D.A., Macías, F., Calvo de Anta, R., Pérez-Alberti,
495 A.,Otero-Pérez, X.L., Verde-Vilanova, J.R., Pérez-Llaguno, C., Saiz-Rubio, R., Díez, E., Bolaños-Guerrón,
496 D., (Eds.), Complejo Básico-Ultrabásico de Capelada-Cabo Ortegal. Andavira Editorial, Santiago de
497 Compostela, pp. 24-30.

498 Pérez-Alberti, A., Trenhaile, A. S. (2015a). Clast mobility within boulder beaches over two winters in
499 Galicia, northwestern Spain. Geomorphology, 248, 411–426.
500 https://doi.org/10.1016/j.geomorph.2015.08.001

501 Pérez-Alberti, A., Trenhaile, A. S. (2015b). An initial evaluation of drone-based monitoring of boulder
502 beaches in Galicia, north-western Spain. Earth Surface Processes and Landforms, 40(1), 105–111.
503 https://doi.org/10.1002/esp.3654

504 Prokešová, R., Kardoš, M., Tábork, P., Medvedová, A., Stacke, V., Chudy, F., 2014. Kinematic behaviour
505 of a large earthflow defined by surface displacement monitoring, DEM differencing, and ERT imaging.
506 Geomorphology 224, 86–101.

507 Prokop, A., Panholzer., 2009. Assessing the capability of terrestrial laser scanning for monitoring slow
508 moving landslides. Nat. Hazards Earth Syst. Sci., 9, 1921–1928.

509 San Claudio Santa Cruz, M. (1997). Tesouros asolagados. Historia dos naufraxios no mar de Galicia. Ed.
510 Lea, Santiago de Compostela.

511 Sturdivant, E. J., Lentz, E. E., Thieler, E. R., Farris, A. S., Weber, K. M., Remsen, D. P., Henderson, R. E.
512 (2017). UAS-SfM for coastal research: Geomorphic feature extraction and land cover classification from
513 high- resolution elevation and optical imagery. Remote Sensing, 9(10). https://doi.org/10.3390/rs9101020

514 Sunamura, T., 1992. Geomorphology of rocky coasts. Wiley, New York.

515 Trenhaile, A.S., 1987. The Geomorphology of Rock Coasts. Clarendon Press, Oxford.

516 Trenhaile, A.S., 2014. Climate change and its impact on rock coasts, in: Kennedy, D. M., Stephenson, W.
517 J., Naylor, L. (Eds), Rock Coast Geomorphology: A Global Synthesis. Geological Society, London,
518 Memoirs, 40, pp. 7–17.

519 Turner, D., Lucieer, A., de Jong, S.M., 2015. Time series analysis of landslide dynamics using an
520 unmanned aerial vehicle (UAV). Remote Sensing 7, 1736–1757.

521 Turner, I.L., Harley, M.D., Drummond, CD. 2016. UAVs for coastal surveying. Coastal Engineering 114,
522 19–24.

523 Vann Jones (née Norman), E. C., Rosser, N. J., Brain, M. J., D. N. 2015. Quantifying the environmental
524 controls on erosion of a hard rock cliff. Marine Geology 363, 230-242.

525 Varnes, D.J. 1978. Slope movement types and processes. In Landslides: Analysis and Control, 11–33.
526 Washington, DC: Transport Research Board, National Academy of Sciences. Special Report.

527 Vericat, D., Brasington, J., Wheaton, J., Cowie, M. (2009). Accuracy assessment of aerial photographs
528 acquired using lighter-than-air blimps: low-cost tools for mapping river corridors. River Research and
529 Applications, 25(8): 985-1000

530 Wheaton, J.M.; Brasington, J.; Darby S.E.; Sear, D.A. (2010). Accounting for uncertainty in DEMs from

531 repeat topographic surveys: improved sediment budgets. Earth Surface Processes and Landforms, 35,

532 136-156. https://doi.org/10.1002/esp.1886.

Table 1. Available data sources and technical information. Where, georeference 1 was done specifically for this study and 0 by the relevant authority. The symbol - refers to unknown data, no data or not applicable (i.e. not valid for this field). Italics are used for unused flights with low image quality. RMSE is the root-mean-square error. UAV scale (S) was calculated through equation: S = mean altitude flight / focal distance of the camera.

Date	Flight name	Scale (cm)	Resolution**	Georef.	Method	GCPs	RMSE
1945-10-08	*Americano A*	*~1/43,000*	*-*	*1*	*Adjust ©ESRI*	*26*	*4.1195*
1956-10-13	Americano B	1/32,000	0.50-1.00	0	-	-	-
1983-11-15	Interministerial	1/18,000	0.25-0.50	1	Spline	41	0.0032
1984-09-12	*Nacional*	*1/30,000*	*0.50-1.00*	*1*	*Spline*	*26*	*0.3942*
1990-09-15	Costas	1/5,000	0.12	1	Spline	45	0.0134
2002-10-28	*Quinquenal*	*1/40,000*	*0.56-1.00*	*1*	*Spline*	*23*	*0.1115*
2005-05-24	PNOA	1/30,000	0.45	0	GNSS	-	≤ 1m
2008-07-22	PNOA	1/20,000	0.25	0	GNSS	-	≤ 1m
2010-08-10	PNOA*	1/20,000	0.25	0	GNSS	-	≤ 1m
2014-09-25	PNOA	1/20,000	0.22	0	GNSS	-	≤ 1m
2016-08-20	UAV	1/100	0.01	1	©APS***	38	0.0689
2017-06-18	PNOA	1/20,000	0.22	0	GNSS	-	≤ 1m
2018-03-03	UAV	1/90	0.01	1	©APS***	19	0.0571

* Orthoimage + LiDAR data.

** Pixel size (GSD) (m).

*** ©Agisoft PhotoScan (georeferencing is based by a model linear obtained from 7 parameters of transformation: 3 translation parameters; 3 of rotation and 1 of scale, Llena et al., 2018).

Table 2. UAV field and image data for 2016 and 2018.

Parameters	2016	2018
Flying height	39.2 m	35.3
No. images	183	278
Drone model	Phantom 3 advanced	Phantom 3 advanced
Camera	Casio FC300S	Casio FC300S
Camera resolution	4000 x 3000	4000 x 3000
Horizontal error	3.16 cm	4.10 cm
Vertical error	3.70 cm	3.00 cm

544 Table 3. Weather stations used in this study.

ID	Station	Location		Distance study area (km)	Missing data (days)	Date	
		Lat (N)	Lon (E)			From	To
1363[a]	Pontes*	43.4462	7.8599	31.63	59	1956-10-13	1975-08-31
1353E[a]	Cedeira	43.6572	8.0466	9.47	0	1975-09-01	1984-10-31
1353[a]	Capelada**	43.6734	7.9856	5.39	31	1984-11-01	2005-12-31
10097[m]	Faladoira	43.5918	7.7887	20.26	0	2006-01-01	2018-03-03

545 * Feb, Dec 1957 data are missing. Substituted with Capelada Station data.

546 ** Aug 2005 data are missing. Substituted with Pontes Station data.

547 [a] State Meteorological Agency (AEMET).

548 [m] Regional Meteorological Agency for Galicia (MeteoGalicia).

549

550 Table 4. Mean rates of movement ($m \cdot yr^{-1}$) of the 8 points on the flow.

Year	Hut	C1	C2	C3	C4	L1	L2	L3	Mean
1956–1983	0.12	0.22	0.21	0.10	0.07	0.23	0.11	0.06	0.14
1983–1990	0.67	0.49	0.53	0.68	0.89	0.58	0.76	0.71	0.67
1990–2005	0.88	0.90	0.86	0.93	0.86	0.80	0.91	0.82	0.87
2005–2008	0.65	0.49	0.5	0.57	0.37	0.59	0.49	0.32	0.50
2008–2010	0.47	0.39	0.57	0.55	0.47	0.32	0.61	0.74	0.52
2010–2014	0.85	0.74	0.78	0.76	0.76	0.71	0.62	0.48	0.71
2014–2016	0.81	0.84	0.89	0.91	0.82	0.96	0.42	0.57	0.77
2016–2017	0.76	0.77	0.91	0.77	1.01	0.46	0.93	1.03	0.83
2017–2018	0.00	0.50	0.50	0.29	0.28	0.29	1.04	1.37	0.53
Mean	0.48	0.50	0.50	0.48	0.47	0.49	0.48	0.43	

551

552

553

554

555

556

557 Table 5. Azimuthal directions of movement for the 8 points on the flow.

Year	Hut	C1	C2	C3	C4	L1	L2	L3
1956–1983	333	338	0	339	336	315	330	298
1983–1990	324	271	318	320	328	323	326	335
1990–2005	338	339	329	339	321	327	335	324
2005–2008	354	358	356	8	16	314	19	41
2008–2010	6	330	306	313	276	318	336	244
2010–2014	332	335	337	343	335	342	291	337
2014–2016	336	348	347	346	350	303	323	308
2016–2017	266	265	269	272	233	326	221	236
2017–2018	-	219	208	153	328	278	273	268

558

559

560 Table 6. Sedimentary balance. For the DoDs, the resolution was 0.5 m^2 and the LoD_{Min} was ± 25 cm.

Sedimentary balance	2010-2016	2016-2018
Total volume of surface lowering	5279	2441
Total volume of surface raising	2042	955
Total volume of LOD_{Min} at ± 25cm	602	1035
Total volume difference	7321	3397
Total net volume difference	-3237	-1486

561

562

563

564

565

566

567

568

569

570 Table 7. Number of consecutive 5- and 10-day events with rainfall totals greater than 150 to 350 mm.

Year	Cumulative 5-day total			Cumulative 10-day total		
	Pr > 150 mm	Pr > 200 mm	Pr > 250 mm	Pr > 250 mm	Pr > 300 mm	Pr > 350 mm
1956–1983	4.9	0.9	0.1	2.4	0.6	0
1983–1990	8.3	2.5	1.3	5.8	1.9	0.4
1990–2005	6.6	0.9	0.1	2.5	0.7	0.3
2005–2008	2.5	0.0	0.0	0.6	0.0	0.0
2008–2010	5.4	2	0.0	0.0	0.0	0.0
2010–2014	2.2	0.0	0.0	0.0	0.0	0.0
2014–2016	8.4	5.3	2.1	10.5	8.4	2.1
2016–2017	0.0	0.0	0.0	0.0	0.0	0.0
2017–2018	11.3	0.0	0.0	0.0	0.0	0.0

571

572

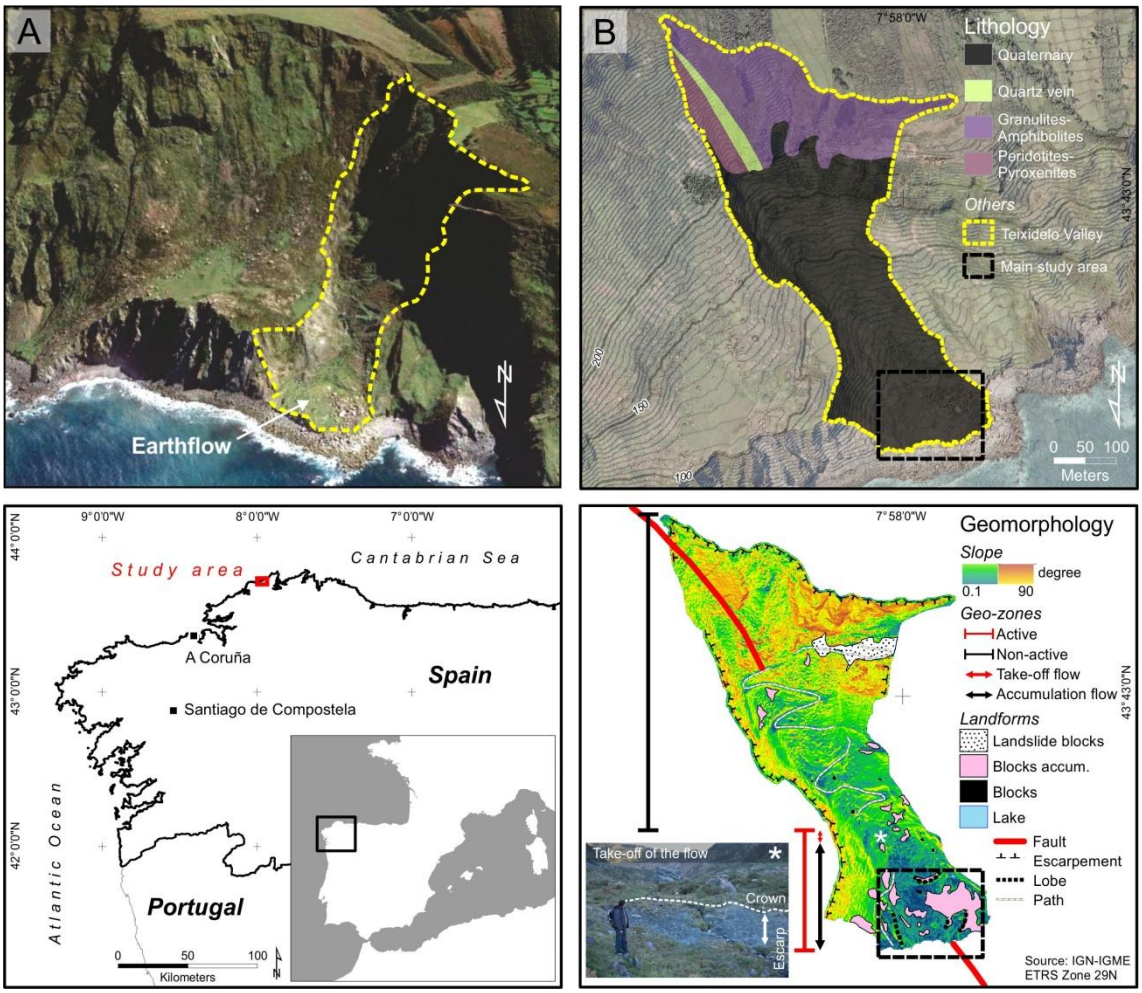

573

574 Figure 1. Oblique image (A) (source GoogleEarth), geological map (B), general location of the study area
575 in northwestern Spain, and its slope and geomorphological characteristics. To avoid relief inversion, (A)
576 and (B) are oriented so that north is at the bottom of the page.

577

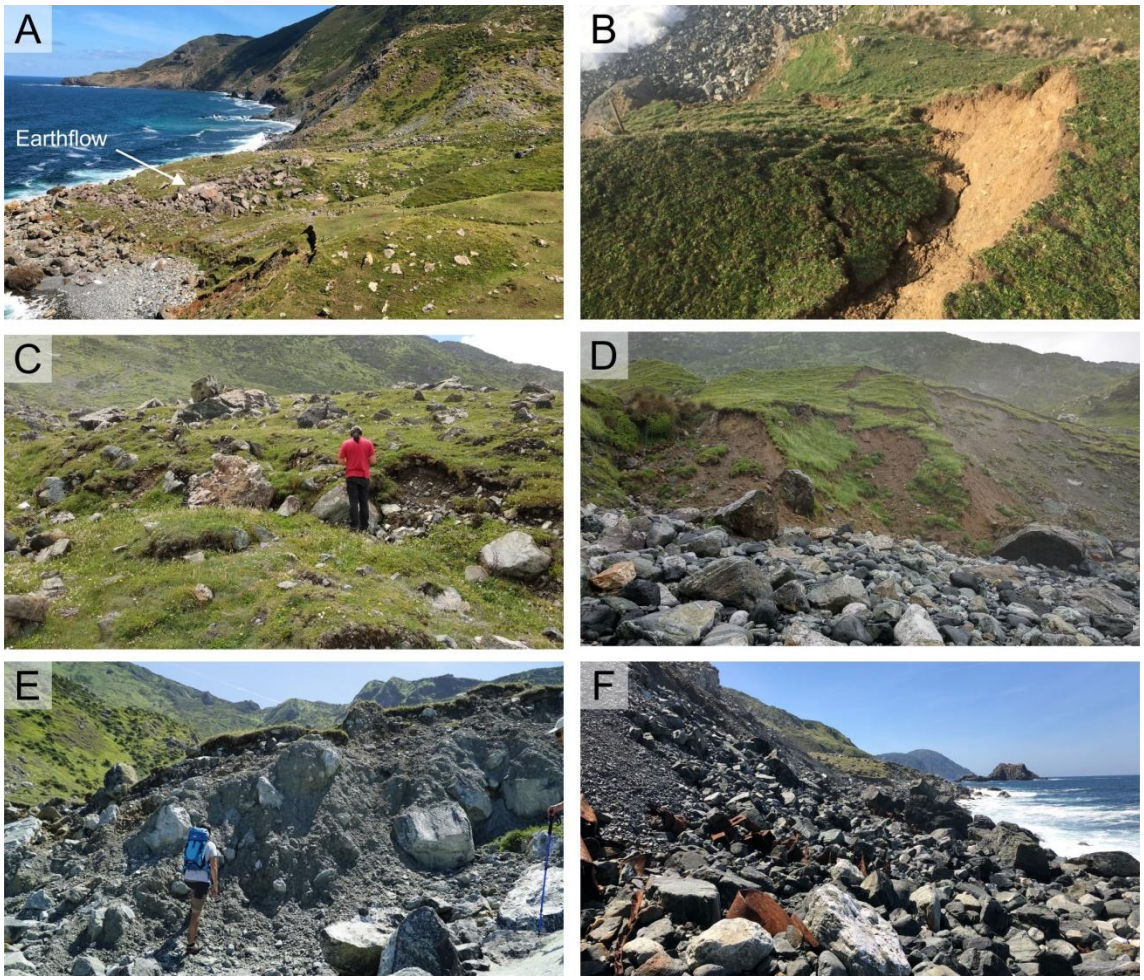

578

579 Figure 2. (A) The earthflow lobe extending to the coast; (B) the arcuate clay scarp at the rear of the zone
580 of depletion; (C) hummocky lobes with exposed boulders in the accumulation zone; (D) the eroded,
581 seaward toe of the flow and the adjacent boulder beach; (E) the eroded toe forming a cliff composed of
582 large clasts in a clay matrix; (F) The coarse boulder beach at the cliff foot.

583

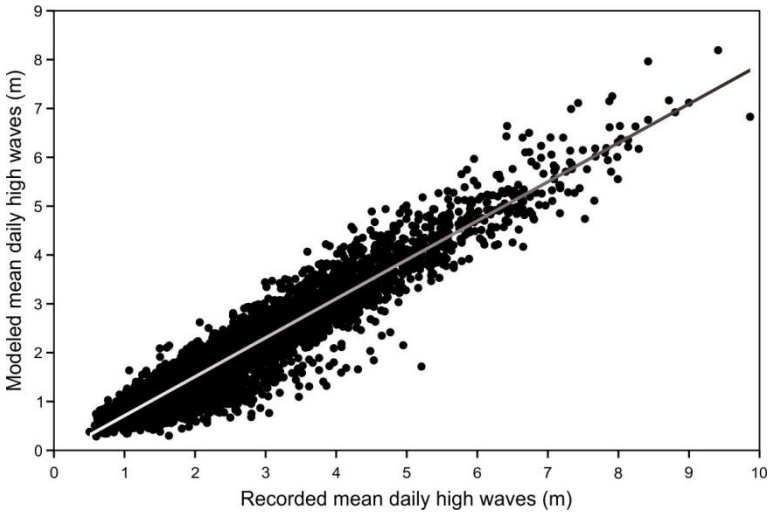

584

585 Figure 3. Mean daily significant wave heights with regression line modeled for SIMAR point 3036042 and
586 recorded at the Estaca de Bares buoy since 1996.

587

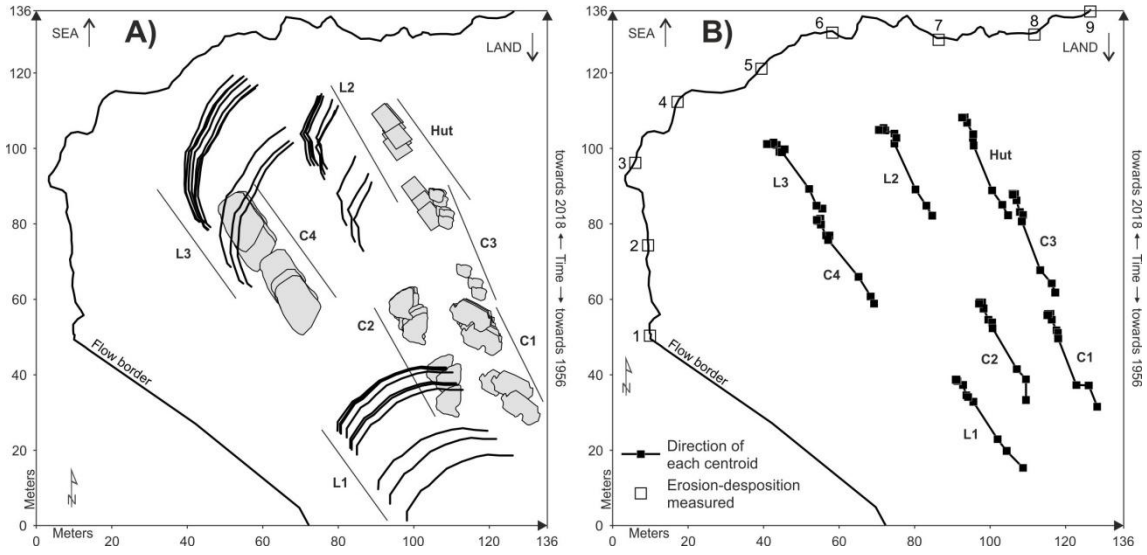

588

589 Figure 4. (A) Recorded location, for each of the monitoring periods, of eight features on the flow from 1956
590 to 2018. They include 4 large boulders (clasts C1 to C4), 3 topographic lobes (L1 to L3), and the
591 foundations of a former hut. The labeled straight lines show the total distance traveled by each feature
592 over the study period. (B) Corresponding changes in the location of the centroids and the transport paths
593 of the eight tracked features. The sites (1 to 9 only, 10 is further east) used to record wave erosion are
594 shown along the coast.

595

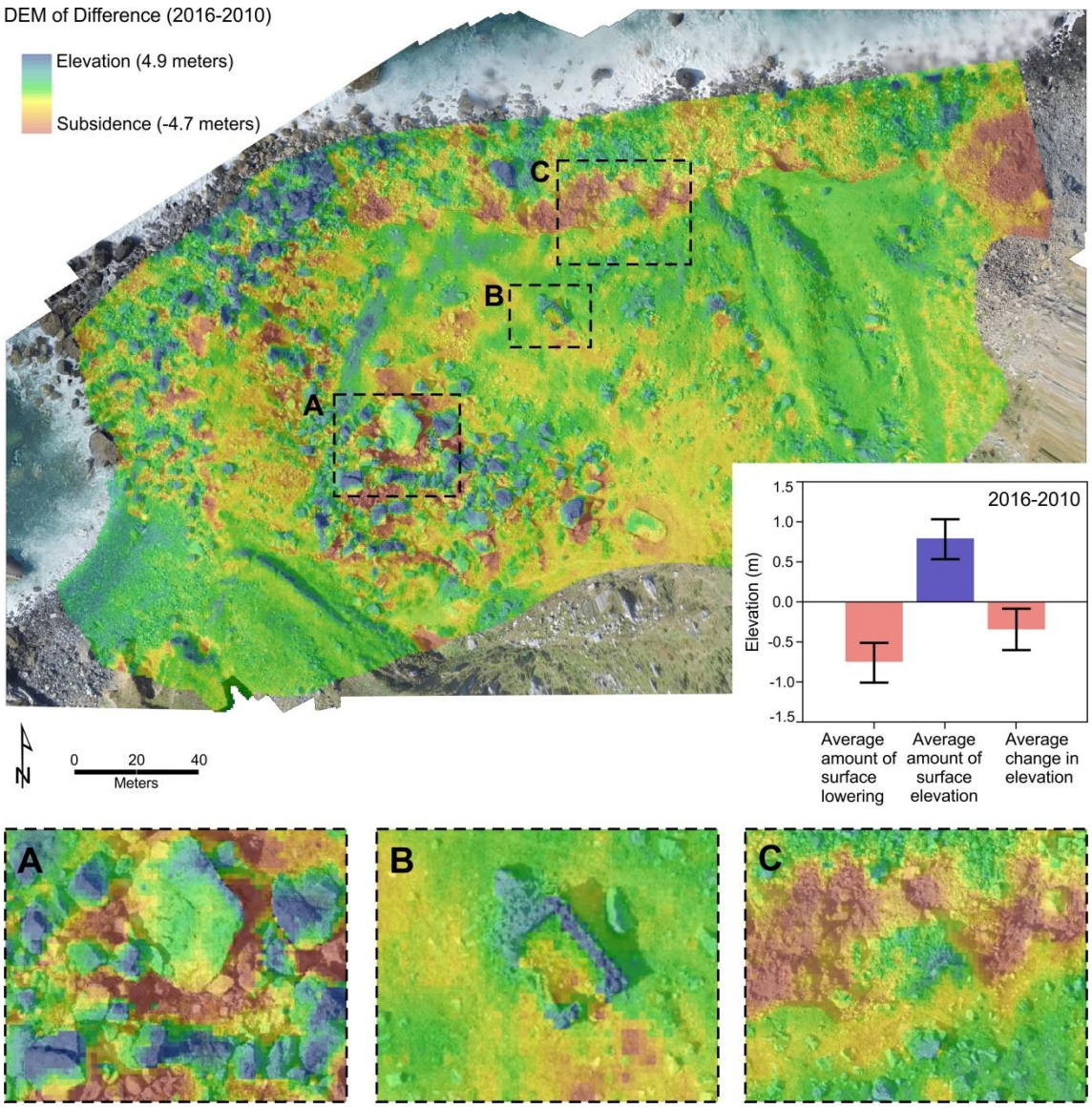

596

597 Figure 5. DEM of difference showing changes in the surface elevation of the flow between 2010 and 2016.

598 A, B, and C provide more detailed information from three sample areas, with summary statistics illustrated

599 in the accompany bar graph.

600

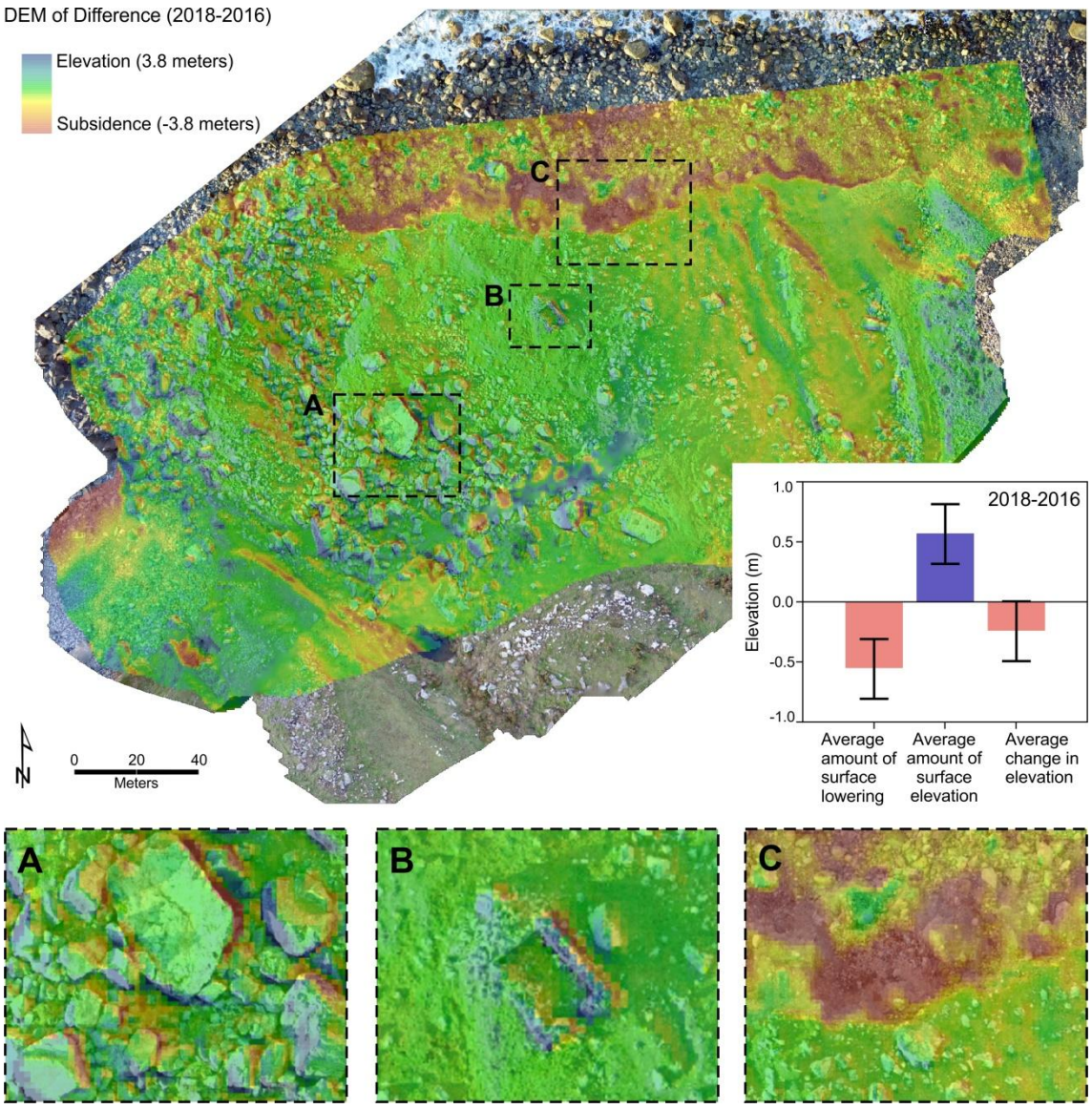

601

602 Figure 6. DEM of difference showing changes in the surface elevation of the flow between 2016 and 2018.
603 A, B, and C provide more detailed information from three sample areas, with summary statistics illustrated
604 in the accompany bar graph.

605

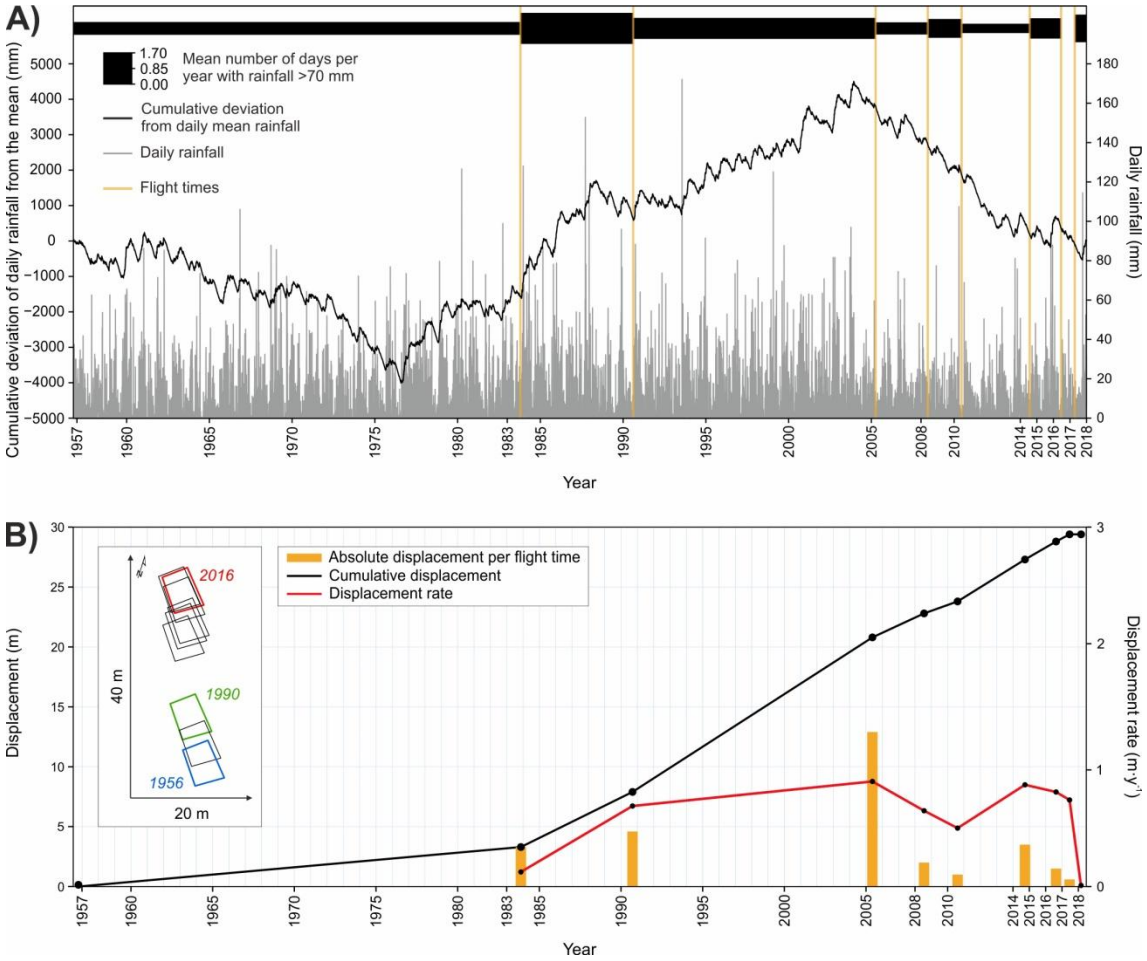

606

607 Figure 7. (A) Daily rainfall and cumulative deviation of daily precipitation from the mean. (B) Earthflow
608 movement over the study period based on the location of the hut which, in contrast to other parts of the
609 flow, did not move from 2017 to 2018.

610

611

612

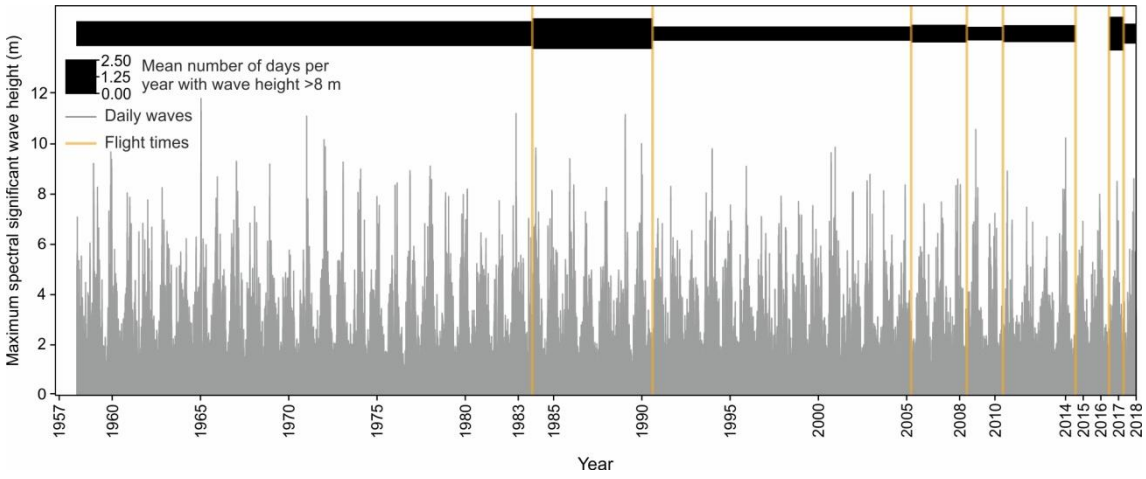

613

614 Figure 8. Maximum spectral significant wave height and the number of days with maximum wave heights >

615 8 m.

616

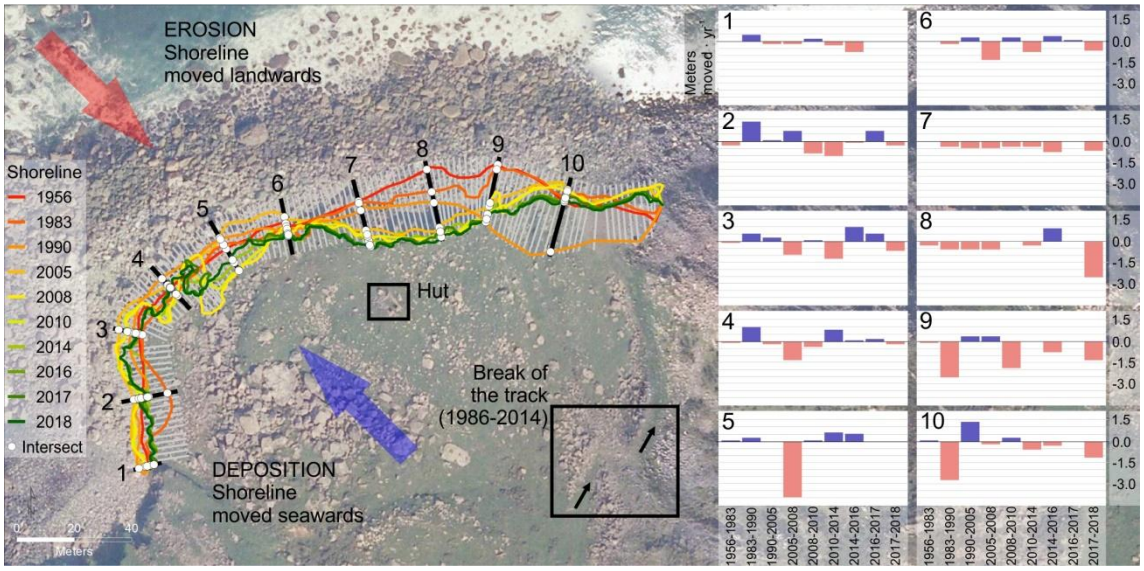

617

618 Figure 9. Mapped and graphed changes in the location of the coast at each of the 10 points (lines) located

619 approximately 24 m apart along the toe of the flow. The break in the road refers to movement of a path

620 (from 1986 to 2018) constructed in order to remove the ship wreck.

621

622

623 Figure 10. The 1986 wreck of the 185 m-long freighter Bonnie Carrier, showing the track and other
624 modifications made to the valley to provide access and to expedite its removal. The images on the left
625 were scanned from Concello de Cariño (2010), and the ones on the right from San Claudio Santa Cruz
626 (1997).

627

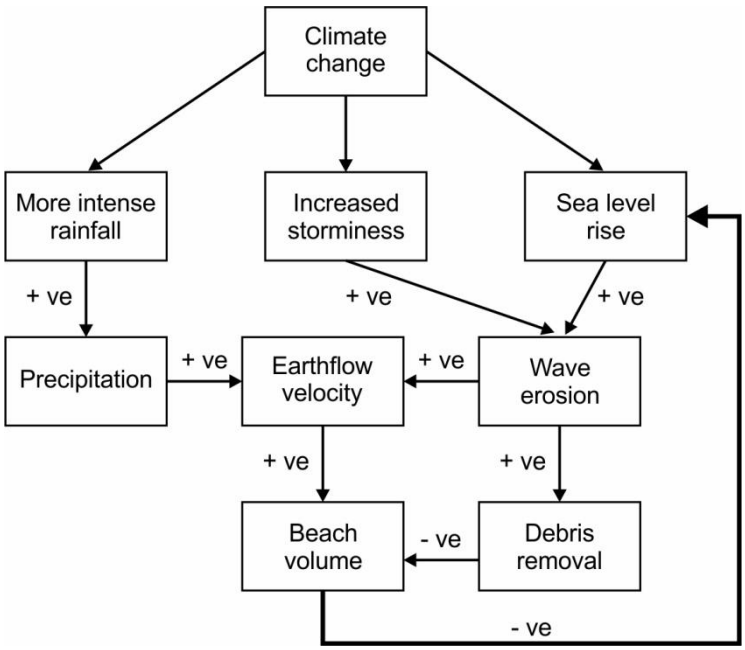

628

629 Figure 11. Possible relationships between earthflow activity and a variety of terrestrial and marine
630 conditions. The thick line represents the negative feedback effect of earthflow velocity, and consequently
631 beach height and volume, on wave erosional efficacy.